optica

Single-crystal diamond low-dissipation cavity optomechanics

Matthew Mitchell,[1,2] Behzad Khanaliloo,[1,2] David P. Lake,[1,2] Tamiko Masuda,[1] J. P. Hadden,[1] and Paul E. Barclay[1,2,*]

[1]Department of Physics and Astronomy and Institute for Quantum Science and Technology, University of Calgary, Calgary, Alberta T2N 1N4, Canada
[2]National Institute for Nanotechnology, Edmonton, Alberta T6G 2M9, Canada
*Corresponding author: pbarclay@ucalgary.ca

Received 24 May 2016; revised 29 July 2016; accepted 29 July 2016 (Doc. ID 263726); published 26 August 2016

Single-crystal diamond cavity optomechanical devices are a promising example of a hybrid quantum system: by coupling mechanical resonances to both light and electron spins, they can enable new ways for photons to control solid-state qubits. However, realizing cavity optomechanical devices from high-quality diamond chips has been an outstanding challenge. Here, we demonstrate single-crystal diamond cavity optomechanical devices that can enable photon–phonon spin coupling. Cavity optomechanical coupling to 2 GHz frequency (f_m) mechanical resonances is observed. In room-temperature ambient conditions, these resonances have a record combination of low dissipation (mechanical quality factor, $Q_m > 9000$) and high frequency, with $Q_m \cdot f_m \sim 1.9 \times 10^{13}$, which is sufficient for room-temperature single-phonon coherence. The system exhibits high optical quality factor ($Q_o > 10^4$) resonances at infrared and visible wavelengths, is nearly sideband resolved, and exhibits optomechanical cooperativity $C \sim 3$. The devices' potential for optomechanical control of diamond electron spins is demonstrated through radiation pressure excitation of mechanical self-oscillations whose 31 pm amplitude is predicted to provide 0.6 MHz coupling rates to diamond nitrogen vacancy center ground-state transitions (6 Hz/phonon) and $\sim 10^5$ stronger coupling rates to excited-state transitions.

OCIS codes: (120.4880) Optomechanics; (140.4780) Optical resonators; (220.1920) Diamond machining; (230.0230) Optical devices.

http://dx.doi.org/10.1364/OPTICA.3.000963

1. INTRODUCTION

Diamond cavity optomechanical devices are an attractive platform for controlling the interactions between light, vibrations, and electrons that underly future hybrid quantum technologies [1]. Their potential arises from diamond's exceptional mechanical and optical properties [2], combined with its ability to host color centers such as the nitrogen-vacancy (NV), whose electron spins are excellent qubits that can be manipulated by local mechanical strain fields [3–7]. Recently, the piezoelectric actuation of bulk [3,8] and nanomechanical [4–7,9–11] diamond resonators has been used to demonstrate phononic spin control. Cavity optomechanics [12] harness optical forces in place of piezoelectric actuation, allowing coherent phonon state manipulation [13–15] of GHz frequency mechanical resonators with quantum limited sensitivity [16]. These phonons can be made resonant with NV center electron spin transitions that are central to proposals for spin–spin entanglement [17], spin-phonon state transfer [18–20], spin-mediated mechanical normal mode cooling [17,21,22], and photon–phonon spin coupling [23]. Additionally, the relatively small thermal occupancy and mechanical dissipation of GHz diamond devices, combined with diamond's ability to support strong optical fields due to its large electronic bandgap, make them an ideal system for the cavity optomechanical backaction cooling and study of mechanical resonators in their quantum ground state [16].

The development of cavity optomechanical devices from single-crystal diamond has been limited due to the challenges associated with fabricating mechanically isolated structures from bulk diamond chips. While the initial development of diamond optomechanical devices used nanocrystalline diamonds [24], single-crystal diamond material promises lower mechanical dissipation [25] and the ability to host highly coherent NV centers [26]. Here, we report the demonstration of a single-crystal diamond cavity optomechanical system for the first time. This system is based on a microdisk device geometry that has been used in a wide range of cavity optomechanics experiments implemented in more conventional semiconductor and dielectric materials [13,15,27,28]. Microdisks are desirable owing to their simple geometry, strong optomechanical coupling between high-frequency mechanical resonances and low-loss optical modes, and intrinsic ability to simultaneously support optical modes over the entire transparency window of the device material [15].

The microdisk system studied here, an example of which is shown in Fig. 1(a), supports optical modes at visible and telecommunication wavelengths ($\omega/2\pi \sim 200$–470 THz) that interact

via radiation pressure with GHz frequency mesoscopic mechanical resonances of the structure. We find that these resonances have a record combination of high ω_m and low mechanical dissipation ($\gamma_m = \omega_m/Q_m \sim 2\pi \times 0.2$ MHz) compared to other mechanical resonators operating in ambient temperature and pressure, and that their $Q_m \cdot f_m = 1.9 \times 10^{13}$ Hz product is sufficiently high to satisfy the minimum criteria for single-phonon coherent behavior [12]. The microdisk optical modes have low dissipation ($\gamma_o = \omega_o/Q_o \sim 2\pi \times 3$ GHz), and owing to the negligible nonlinear absorption in diamond at telecom optical frequencies, they can support an intracavity photon number $N > 10^6$ without degrading Q_o. In combination, this allows for the realization of optomechanical cooperativity, $C = Ng_0^2/\gamma_o\gamma_m \sim 3$, large enough (>1) for coherent photon–phonon coupling [13,14], where $g_0 \sim 2\pi \times 26$ kHz is the single photon optomechanical coupling rate of the device and describes the expected shift in the cavity optical frequency due to the mechanical zero-point motion of the microdisk. These devices operate on the border of the sideband-resolved regime ($\gamma_o \sim \omega_m$), enabling radiation pressure backaction excitation of mechanical self-oscillations with ~31 pm amplitude. The accompanying stress fields are strong enough to drive diamond color center spin transitions with a single phonon-spin coupling rate that is predicted to exceed that of previously studied MHz frequency nanomechanical structures [5–7], despite having orders of magnitude higher ω_m and smaller phonon amplitude, owing to the localized nature of the microdisk mechanical resonances. In addition, the ability of the microdisks to support optical modes at visible wavelengths is compatible with resonant coupling to NV center optical transitions [29], as well as operation in fluid environments of interest for sensing applications [27].

2. FABRICATION OF SINGLE-CRYSTAL DIAMOND MICRODISKS

There has been significant recent progress in the fabrication of mechanically isolated single-crystal diamond devices, including demonstrations of suspended high-Q_m nanomechanical resonators [4,25,30–32] and high-Q_o micro- and nanocavities [33,34]. These structures have been created using diamond membrane thinning [25,30,35], plasma angled etching [33], and plasma undercutting [32,34] fabrication techniques, with the latter two approaches allowing for the patterning of devices from bulk diamond chips. Here, we use plasma undercutting to fabricate single-crystal diamond cavity optomechanical devices [32,34]. These devices were fabricated from an optical grade, chemical vapor deposition (CVD)-grown ⟨100⟩-oriented single-crystal diamond substrate supplied by Element Six. The polished substrates were first cleaned in boiling piranha and coated with ~400 nm of plasma-enhanced chemical vapor deposition (PECVD) Si_3N_4 as a hard mask. To avoid charging effects during electron beam lithography (EBL), ~5 nm of Ti was deposited on the Si_3N_4 layer before coating the sample with a ZEP 520A EBL resist. The developed pattern was transferred to the hard mask via inductively coupled plasma reactive-ion etching (ICPRIE) with C_4F_8/SF_6 chemistry. The remaining EBL resist was removed with a 6 min deep-UV exposure (5 mW/cm^2 at 254 nm), followed by a 2 min soak in Remover PG, while the remaining Ti was removed by the subsequent etch steps. The anisotropic ICPRIE diamond etch was performed using O_2, followed by the deposition of ~250 nm of conformal PECVD Si_3N_4 as a sidewall protection layer. The bottom of the etch windows were then cleared of Si_3N_4 using a short ICPRIE C_4F_8/SF_6 etch. This was followed by a zero RF power O_2 RIE diamond undercut etch to partially release the devices. Lastly, the Si_3N_4 layer was removed using a wet etch in 49% HF, and the devices were cleaned again in boiling piranha. The devices studied here have diameters of 5.0 to 6.0 μm and an average thickness ~940 nm. As evident from the image in Fig. 1(a), the devices are fabricated with a process optimized to minimize the waist of the pedestal supporting the microdisk, reducing it to <100 nm, where the waist is defined as the smallest point of the pedestal. The microdisk thickness, which will be reduced in future work to enhance confinement, is determined by the interplay between the inward and upward etch rates of the quasi-isotropic undercut, together with the initial anisotropic etch depth. The undercut time was chosen to optimize the pedestal waists of the ~5 μm diameter microdisks studied here. A longer undercut would allow the study of larger diameter microdisks (from 6 to 8 μm) present on the chip, which would in turn possess a smaller thickness than the structures studied here.

3. DEVICE CHARACTERIZATION

A. OPTICAL CHARACTERIZATION

The devices were characterized by monitoring the transmission of a dimpled optical fiber taper [36,37] evanescently coupled to the

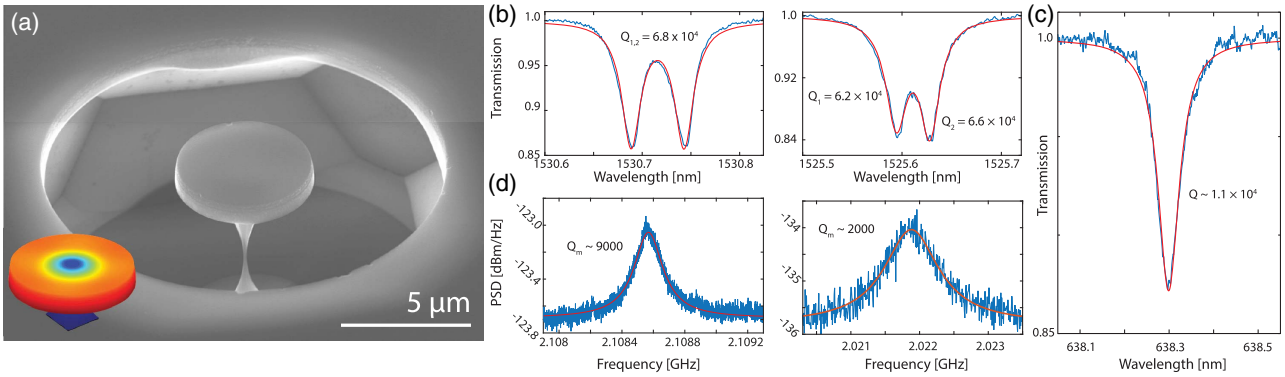

Fig. 1. Characterization of diamond microdisk optical and mechanical modes at low optical input power. (a) SEM image of a 5 μm diameter microdisk, with minimum pedestal width of 100 nm. Inset: Simulated displacement distribution of the RBM mechanical resonance of this device. (b) Highest Q_o TM-like optical modes of a 5 μm (left) and 5.5 μm (right) diameter microdisk, with intrinsic quality factors for each doublet resonances, as labeled. (c) High-Q_o visible mode with intrinsic quality factor, as shown for a 6.2 μm diameter microdisk. (d) $S_P(f)$ produced by the thermal motion of the RBM of the microdisks in (b), showing that the larger diameter, larger pedestal waist microdisk has a lower Q_m.

microdisk and input with light from tunable diode lasers (New Focus Velocity) with wavelengths near 1530 or 637 nm. For the 1530 nm measurements, the output of the fiber taper was monitored by both low- and high-bandwidth photoreceivers (Newport 1621 and 1554-B, respectively) and a calibrated optical power meter (Newport 2936-R). Figure 1(b) shows typical $\overline{T}(\lambda_s)$ when the fiber taper is evanescently coupled to devices with diameters of 5.0 and 5.5 μm and the wavelength λ_s of the 1530 nm tunable laser is scanned across microdisk modes at λ_o. Here, $\overline{T}$ is the average transmission measured by the low-bandwidth photodetector over a timescale that is long compared to $1/f_m$. These measurements reveal resonant coupling to modes with loaded $Q_o \sim 5.8 \times 10^4$–6.0×10^4 (intrinsic $Q_o^{(i)} = 6.1 \times 10^4$–$6.8 \times 10^4$) and a degree of doublet structure that depends on the internal backscattering of a given device. Maximizing Q_o, and thereby minimizing γ_o, is important for achieving the aforementioned regime and allowing coherent photon–phonon coupling ($C > 1$).

The ability of these devices to support modes over a wide wavelength range is demonstrated in Fig. 1(c), where the 637 nm tunable laser was used to probe a mode with a high $Q_o > 1 \times 10^4$. This is promising for applications involving NV center optical transitions in this wavelength range [10]. These devices have a predicted radiation loss-limited $Q_o > 10^7$ at both 1550 and 637 nm wavelengths; γ_o is currently limited by the surface roughness and linear absorption. In a previous work, the microdisk pedestal size was observed to limit Q_o for insufficient relative undercut. In the devices studied here, scattering due to the non-cylindrical pedestal shape is predicted to dominate the contribution to γ_o from the pedestal [34]. The lower Q_o observed at 637 nm can be attributed in part to sub-optimal fiber taper positioning [38] and an increased sensitivity to surface scattering [33].

B. CAVITY OPTOMECHANICAL COUPLING

To probe optomechanical coupling within the microdisks, time (t) -dependent transmission fluctuations $\delta T(t, \lambda_s)$ of 1550 nm light were monitored using a real-time spectrum analyzer (Tektronix RSA5106A). Excitations of the microdisk mechanical resonances modulate λ_o, resulting in a dispersive optomechanical transduction of mechanical motion to an optical signal $P_o \delta T(t; \lambda_s)$ that can then be observed in the measured electronic power spectrum $S_P(f)$. Here, P_o is the average power transmitted to the photoreceiver. Figure 1(d) shows typical spectra when λ_s is tuned near the point of maximum transduction of the modes in Fig. 1(b). Resonances near $f_m \sim 2.0$–2.1 GHz are observed, corresponding to optomechanical transduction of the thermomechanical motion of the fundamental radial breathing mode (RBM) of the microdisks. The predicted displacement of the RBM calculated using finite element simulations (COMSOL) is shown in the inset of Fig. 1(a). The simulated f_m of the RBM for varying microdisk diameters was found to be within 10% of the observed values. These measurements were conducted at a low input power $P_i \sim 50$ μW to avoid the optomechanical backaction effects discussed below. Here, an erbium-doped fiber amplifier (EDFA: Pritel LNHPFA-30) was used on the output side of the fiber taper to boost the optical signal prior to photodetection to a level just below the detector saturation power ($P_o \approx 0.7$ mW).

The microdisk pedestal can significantly affect the RBM properties, and minimizing its waist size is important in order to maximize Q_m and reach $C > 1$. In previously studied diamond microdisks with μm pedestal waists [34], the transduction of mechanical modes was not observed. As shown in Fig. 1(a), the devices used here for cavity optomechanics have significantly smaller waists, e.g., the 5.0 μm diameter microdisks have waist <100 nm. Figure 1(d) shows that when the microdisk diameters, and as a result, the pedestal waist are increased to 5.5 μm and 400 nm, respectively, Q_m is found to decrease from ∼9000 to ∼2000. Mechanical resonances are not observed in devices with a pedestal diameter >500 nm. This indicates that Q_m for these devices is limited by clamping loss [28,39]. The hourglass shape of the pedestals obtained for the ⟨100⟩ optical-grade diamond samples used here limits the minimum size of the pedestal where it connects to the microdisk and may result in increased dissipation. Given the crystal plane selective nature of the diamond undercut [34], fabricating microdisks from samples with alternate crystal orientations such as ⟨111⟩ may alleviate this limitation. Additionally, an operation in a vacuum, where viscous air damping can be avoided [40,41], and at low temperature [25,32] would allow a decrease in dissipation, as the total Q_m is given by $Q_m = (\sum_j 1/Q_m^j)^{-1}$, where Q_m^j represents the quality factor due to each damping mechanism. Despite the present limitations, the demonstrated devices have $Q_m \cdot f_m = 1.9 \times 10^{13}$ Hz, which is larger than all previously studied cavity optomechanical systems operating in ambient conditions [28,39,42]. A comparison of some of the highest $Q_m \cdot f_m$ products for optomechanical systems observed in ambient, cryogenic, and low-pressure environments is shown in Supplement 1, Section 3. This figure of merit is critical for cavity optomechanical mass spectroscopy [27,43,44] and low phase noise oscillators [45]. Within the context of quantum optomechanics, this product satisfies a key minimum requirement for room-temperature studies of single-phonon coherence by over an order of magnitude: $\omega_m/\gamma_m \gg n_{th}$, where n_{th} is the room temperature phonon population of the RBM, ensuring that thermal decoherence is slow compared to a mechanical oscillation [12]. By satisfying this condition, cooling to the quantum ground state from room temperature should also be possible [46].

To investigate the response of the cavity optomechanical transduction, S_P was monitored while λ_s was scanned across λ_o. Figure 2(a) shows the resulting measurement of $S_P(f, \lambda_s)$ for the microdisk in Fig. 1(a), clearly illustrating that optomechanical transduction is only observable when λ_s is tuned in the vicinity of λ_o. In this measurement, the EDFA was connected to the input side of the fiber taper, resulting in maximum $N \sim 6.5 \times 10^5$ and $P_d \sim 1.5$ mW, where P_d is the optical power dropped into the microdisk mode. From the thermo-optic coefficient of diamond, we estimate that the shift of 400 pm from the cold cavity λ_o, as seen in Figure 2(a), corresponds to a change in device temperature $\Delta T \sim 50$ K. The COMSOL simulations that take into account the reduced thermal conductivity coefficient of the ∼100 nm diameter pedestal compared to bulk [47] confirm that an absorbed power of ∼10% of P_d reproduces the temperature shift observed here (see Supplement 1, Section 1). Although this temperature increase is not desirable for quantum optomechanics applications, it is considerably smaller than the expected increase for a similar Si device. Assuming a similar absorption rate and identical device geometry, a silicon device with a silicon or silicon dioxide pedestal would result in $\Delta T \sim 200$ K or 450 K, respectively, where a modified thermal conductivity also applies to the silicon in the pedestal [48]. It is expected that the rate of linear absorption observed here, which corresponds to $Q_o^{abs} = 6.2 \times 10^5$, can be reduced through improvements in processing,

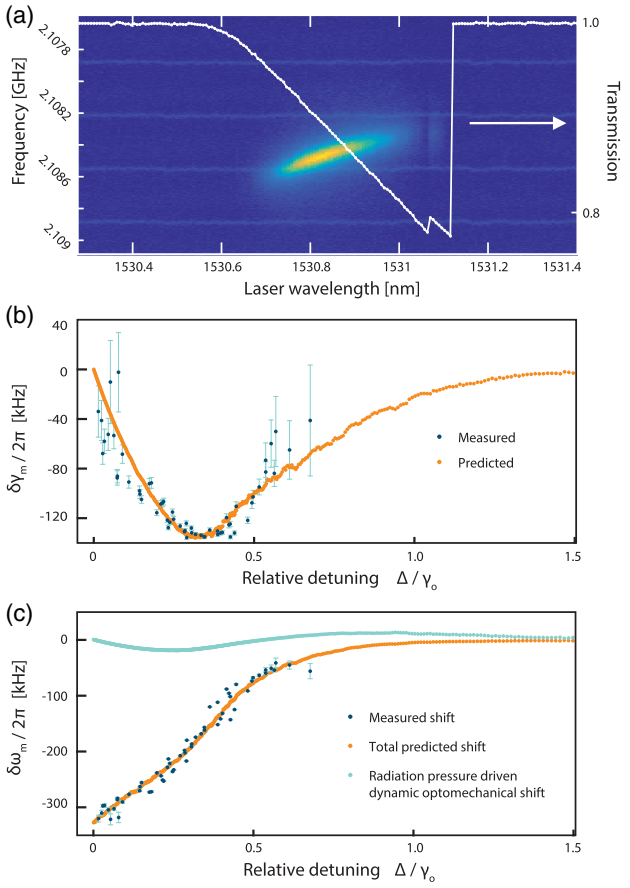

Fig. 2. Optomechanical backaction measuerments. (a) $S_P(f, \lambda_s)$ and corresponding fiber transmission $T(\lambda)$ for P_i corresponding to maximum $N \sim 6.5 \times 10^5$ and $P_d \sim 1.5$ mW. The regularly spaced horizontal features are electronic noise from the apparatus. (b) Observed and predicted optomechanical linewidth narrowing of the RBM. The predicted $\delta\gamma_m$ depends on measured N and Δ for each point, as well as fitting parameter $g_0/2\pi = 26 \pm 2$ kHz. Error bars indicate 95% confidence interval for γ_m extracted from $S_P(f)$ at each data point. (c) Observed and predicted $\delta\omega_m$. Both the predicted shift due to optomechanical backaction for g_0 found from the fits in (b) and the predicted shift, including an additional static thermal softening determined by a free-fitting parameter, are shown.

as diamond devices with $Q_o > 10^6$ have been reported elsewhere [49].

C. CAVITY OPTOMECHANICAL BACKACTION

The influence of cavity optomechanical backaction [12] on the dynamics of the mechanical resonator is analyzed in Figs. 2(b) and 2(c). The changes from $\delta\gamma_m$ and $\delta\omega_m$ to γ_m and ω_m, respectively, were measured as a function of source-cavity detuning $\Delta = \omega_s - \omega_o$. Their strong dependence on Δ clearly indicates that the mechanical dynamics are affected by the intracavity field. We were prevented from measuring significant $\delta\gamma_m$ and $\delta\omega_m$ for red-detuned wavelengths ($\Delta < 0$) due to the thermal bistability present in our system for large P_d, as shown in Fig. 2(a). As such, this study concentrated on blue-detuned wavelengths ($\Delta > 0$); however, the implementation of cavity stabilization techniques [15] may allow this limitation to be overcome in the future, enabling more effective investigations of cavity sideband cooling [12,16] and optomechanically induced transparency [13–15]. Determining Δ for each data point in this analysis required accounting for the dependence of ω_o on N due to the thermo-optic effect. For a given operating ω_s, ω_o was predicted from N (see Supplement 1, Section 1), where $N(\omega_s)$ was determined from $\overline{T}(\omega_s)$, P_i, $Q_o^{(i)}$ and measurements of loss through the fiber taper and other elements of the apparatus.

To quantitatively investigate the role of radiation pressure on the mechanical resonance dynamics, the observed $\delta\gamma_m(\Delta)$ was fitted to the expected cavity optomechanical damping rate [12], with the single-photon optomechanical coupling rate g_0 as the only free parameter. Using this method, the fit shown in Fig. 2(b) was obtained for $g_0/2\pi \sim 26$ kHz, with an associated 95% confidence interval of ± 2 kHz. The errors bars for each $\delta\gamma_m$ data point in Fig. 2(b) represent the 95% confidence interval of fits used to extract γ_m from S_P. The large uncertainty as well as the discrepancy between the measured and predicted values when $\Delta \sim 0$ or $\gg\gamma_o$ are due to the low signal to noise of S_P in these regions. This low signal to noise of S_P also prohibited measuring the optomechanical response for $\Delta \gg \gamma_o$. The fitted value for g_0 has good agreement with the value of g_0 predicted from the COMSOL calculations, which include both moving boundary (MB) and photoelastic (PE) contributions [50]. The predicted g_0 is dependent on the spatial overlap of the optical field and mechanical displacement profile, which varies for each optical mode. We find that the fitted value of g_0 most closely agrees with the predicted coupling rate of the second-order radial TM-like mode, with $g_{0_{PE}}/2\pi = 18$ to 24 kHz and $g_{0_{MB}}/2\pi = 16$ kHz. In comparison, $g_{0_{MB}}/2\pi = 17$ kHz (19 kHz) and $g_{0_{PE}}/2\pi =$ 29 to 36 kHz (−24 to −26 kHz) for the fundamental TM (TE) mode of the microdisk. This is consistent with the measurements of the mode polarization in the fiber taper, which indicated that the microdisk mode studied here is TM polarized. Note that the stated uncertainty in the predicted $g_{0_{PE}}$ is due to variations in the reported PE coefficients of single-crystal diamond [51].

Figure 2(c) shows a similar analysis of $\delta\omega_m(\Delta)$, indicating that ω_m is softened by over 300 kHz by the intracavity field. This shift is due to both optomechanical dynamical backaction and static thermal effects. For the operating regime and devices used here, the dynamic thermal effects are expected to be below 5% of the optomechanical radiation pressure dynamical backaction effects and can be neglected [42]. However, the static thermal effects are significant. Heating of the microdisk for a large P_d results in both thermal expansion and a change in Young's modulus, resulting in a shift to ω_m [52–54]. This effect is linear in P_d, assuming that Q_o is independent of power, i.e., the nonlinear absorption is small. To compare the measured $\delta\omega_m(\Delta)$ with the theory, we used a model that includes radiation pressure-induced optomechanical dynamic backaction [12] and a static heating term linearly proportional to P_d:

$$\delta\omega_m(\Delta) = g_0^2 N\left(\frac{\Delta - \omega_m}{\gamma_o^2/4 + (\Delta - \omega_m)^2} + \frac{\Delta + \omega_m}{\gamma_o^2/4 + (\Delta + \omega_m)^2}\right) + \alpha P_d. \quad (1)$$

The resulting fit of Eq. (1) to the measured $\delta\omega_m$ is shown in Fig. 2(c) to have a close agreement. Notably, this model reproduces the kink in $\delta\omega_m(\Delta)$, where the amplitude of the optomechanical contribution reaches a maximum and changes signs. This fit was obtained with g_0 fixed to the value extracted from the analysis of $\delta\gamma_m$ in Fig. 2(b) and with α as a fitting parameter.

At higher powers, the microdisk optomechanical dynamics can be dramatically modified. Figure 3 shows the behavior of the

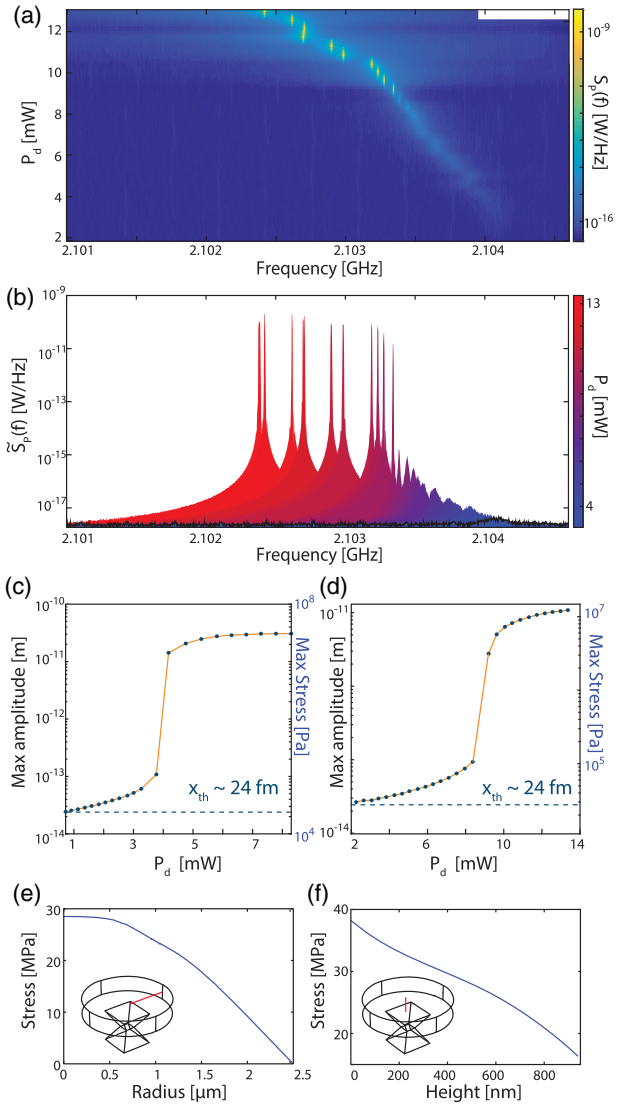

Fig. 3. Observation of microdisk self-oscillation. (a) $S_P(f;\lambda_{opt})$ as a function of dropped power. (b) Normalized cross sections of (a), where $\tilde{S}_P(f)$ is given by $S_P(f;\lambda_{opt})$ normalized by the transduction gain so that the area under the curve represents the mechanical energy of the RBM. The black data is the thermal displacement spectra. (c, d) Maximum displacement amplitude and stress for 5 μm diameter devices with (c) $Q_m \sim 9000$, $Q_o^{(t)} \sim 6\times10^4$, and (d) $Q_m \sim 8000$, $Q_o^{(t)} \sim 4\times10^4$. (e, f) Simulated stress along (e) radial and (f) vertical cuts in the microdisk, as indicated by the red lines in the insets, for the self-oscillating amplitude in (c).

microdisk RBM when the input power to the fiber taper is increased sufficiently for P_d to reach 13 mW. This elevated power level corresponds to an intracavity photon number $N \sim 2.8\times10^6$ and an optomechanical cooperativity $C = Ng_0^2/\gamma_o\gamma_m = 2.7$ for the device shown in Fig. 1(a). This C exceeds all previously reported values for devices operating in ambient conditions [14,15]. For such large P_d, if the input λ_s is appropriately blue detuned from λ_o, it is possible for $\delta\gamma_m + \gamma_m \to 0$, resulting in the self-oscillation of the microdisk RBM. Operation in this regime results in large dynamical strain within the microdisk, offering a potential path for achieving for large NV spin-phonon coupling.

We predict the strain achievable in our devices from measurements as follows. The microdisk mechanical response in the transition from thermal motion to self-oscillation is shown in Fig. 3(a), which displays $S_P(f;\lambda_{opt})$ for varying P_d, with λ_s tuned to the value λ_{opt}, where $S_P(f_m)$ is the maximum. As P_d is increased, the mechanical resonance is observed to narrow and increase in amplitude, suggestive of the onset of self-oscillations, also referred to as phonon lasing. This is more clearly illustrated in Fig. 3(b), which shows the normalized spectrum $\tilde{S}_P(f)$ for varying P_d. Here, $\tilde{S}_P(f)$ has been obtained by normalizing $S_P(f;\lambda_{opt})$ with the power-dependent transduction gain, such that the area under $\tilde{S}_P(f)$ represents the mechanical energy of the RBM, i.e., $\tilde{S}_P$ is constant with respect to P_i in the absence of optomechanical backaction (see Supplement 1, Section 2). At low powers, this mechanical energy is dominantly from the thermal bath and is predicted from the equipartition theorem to correspond to the oscillation amplitude $x_{th} \sim 24$ fm. Figures 3(c) and 3(d) show that for large P_d, a maximum $x_{om} = 31$ pm is reached, likely limited by the nonlinearity of the material. The corresponding predicted maximum stress associated with the self-oscillations, also shown in Figs. 3(c) and 3(d), is >30 MPa. The stress values were determined from x_{om} and the finite element simulations of the RBM displacement field shown in Fig. 1(a), and the maximum is predicted to occur at the center of the microdisk's top surface, as shown by the plots in Figs. 3(e) and 3(f). The corresponding maximum strain is $\approx 30\times10^{-6}$.

The self-oscillation threshold behavior can be quantitatively analyzed by extracting the mechanical displacement amplitude x_{om} as a function of P_d from $\tilde{S}_P$. This is shown in Figs. 3(c) and 3(d) for two similarly sized microdisks. In each case, a clear threshold is observed. Since these microdisks have different Q_m and Q_o (see Fig. 3 caption), their threshold powers P_T differ. For devices close to the sideband-resolved regime, the optimal detuning for self-oscillation to occur is $\Delta \sim \omega_m$, and P_T is given by [55]

$$P_T = \frac{m_{eff}\omega_o}{2g_{om}^2}\frac{\gamma_m\gamma_o^{(i)}}{\omega_m\gamma_o^{(t)}}(\gamma_o^{(t)}/2)^2[(2\omega_m)^2 + (\gamma_o^{(t)}/2)^2], \quad (2)$$

where $g_{om} = g_0/x_{zpm}$ is the optomechanical coupling coefficient, and $\gamma_o^{(i)}$ and $\gamma_o^{(t)}$ are the intrinsic and fiber taper-loaded optical decay rates, respectively. Here, $x_{zpm} = \sqrt{\hbar/2m_{eff}\omega_m}$ is the mechanical zero-point motion amplitude. For the devices studied here, $x_{zpm} \sim 0.32$ fm, as calculated from the RBM effective mass $m_{eff} \sim 40$ pg, predicted by the finite element-simulated displacement field shown in Fig. 1(a) [12]. The observed $P_T = 3.5$ and 8.5 mW, for the devices in Figs. 3(c) and 3(d) respectively, are above the predicted values of 760 μW and 3.0 mW obtained from Eq. (2), assuming g_0 is given by the fits in Fig. 2. This disagreement could be related to the uncertainty in γ_o given that P_T scales to the fourth power of this quantity, the interplay between doublets that is ignored by Eq. (2), and the uncertainty in Δ inferred from the cavity response in the presence of thermo-optic dispersion.

4. DEVICE POTENTIAL FOR HYBRID SPIN-OPTOMECHANICS

The potential of these devices for hybrid spin-optomechanics applications can be measured by the predicted strain coupling rate g_{e^-} between a single phonon of the microdisk RBM and a single-diamond NV center electron spin. The maximum zero-point motion strain of the RBM is $\varepsilon_{zpm} \approx 3\times10^{-10}$, and we estimate $g_{e^-}/2\pi = d\varepsilon_{zpm} \approx 6$ Hz for a negatively charged NV^- center

electron spin optimally located 50 nm below the top surface of the device in Fig. 3(c), exceeding the highest rate demonstrated to date [7]. Here, $d \approx 10$–20 GHz is the strain susceptibility of the ground-state spin [5,6]. When the RBM is self-oscillating, as in Fig. 3(c), the predicted coupling rate is $G/2\pi \approx 0.6$ MHz [5]. This is comparable to coupling rates achieved in piezoelectric actuated nanomechanical [5–7] and bulk devices [3,8]. The longest room-temperature ground-state spin decoherence time (T_2) observed to date in an isotopically engineered single-crystal diamond is 1.8 ms [26], while typical T_2 values in nanostructures are on the order of 100 μs [5,56]. Additionally, dynamical decoupling schemes can be utilized to extend this time, as $T_2 \sim 600$ ms has been observed at low temperatures [57]. Phonon-spin control should be possible provided $G/2\pi > T_2$, which is the case for these devices.

The GHz frequency of the RBM enables low room-temperature phonon occupation, relevant for cooling to the quantum ground state from room temperature [16]. This also enables access to larger energy spin transitions [3,8] than were possible using the previously demonstrated diamond nanomechanical resonators. This may be particularly important for future studies of phonon coupling to the NV^- center excited-state manifold, which could achieve single-phonon coupling rates close to MHz due to the $\sim 10^5$ times larger strain susceptibility of the excited states [10,22,58,59]. This is promising for implementing fully quantum photon–phonon–spin interfaces and for proposals of the spin-mediated cooling of nanomechanical resonators [17,21,22].

In the samples under study, we expect to find NVs optimally coupled to the RBM since the nitrogen concentration for this diamond sample (∼ppm, corresponding to a number density of 1.76×10^5 μm^{-3}) results in high-concentration NV ensembles. However, future studies with higher purity samples may require NV implantation to optimally locate NVs ∼ 50 nm below the device surface. Additionally, due to the minimal coupling of fluorescence from an NV center located at the center of the microdisk to the optical modes, free space collection would most likely be required. However, the use of higher-order radial breathing modes could allow for greater spatial overlap of the strain and electromagnetic field maxima [60], allowing for more efficient fiber-based excitation and collection.

Future improvements of Q_o to values above 10^5 and approaching 10^6 should be possible [33,34], thus enabling ultralow self-oscillation threshold [55] and operation deep in the sideband-resolved regime required for optomechanical ground-state cooling [16]. Operating in a vacuum, at a low temperature, and using devices fabricated from high-purity electronic-grade diamonds may allow further increases in Q_m [25], boosting the achievable photon–phonon cooperativity C and $Q_m \cdot f_m$ product. Similarly, reducing the microdisk diameter may increase C through enhanced g_0 while also increasing ω_m. Simulations predict that diameters close to 3.5 μm are possible before radiation loss limits $Q_o < 10^5$; such devices would have $g_0/2\pi > 95$ kHz and $f_m \sim 3.4$ GHz. Finally, using electronic-grade diamond materials and investigating processing techniques to reduce surface-state absorption may decrease optical absorption and allow larger N before device heating becomes significant.

5. CONCLUSION

In conclusion, we have shown that cavity optomechanical devices can be realized from single-crystal diamond, with record high ambient condition optomecanical cooperativity, $C \sim 3$, and a $Q_m \cdot f_m$ product of 1.9×10^{13}. These devices are a promising testbed for ambient-condition coherent optomechanics experiments, e.g., ground-state cooling [16], optomechanically induced transparency [13–15], and phonon-mediated wavelength conversion [15,61,62], as well as studies in quantum information science [63], and hybrid quantum systems involving light, phonons, and diamond NV center spins [3,5–7,17,21,23]. We have also shown that the microdisks demonstrated here support high-Q_o optical modes at wavelengths near resonance with the 637 nm optical transition of NV centers, further enhancing their potential for photon–phonon spin coupling experiments.

We note that, in parallel to this work, Burek *et al.* have demonstrated cavity optomechanics in single-crystal diamond optomechanical crystals fabricated by a Faraday cage angled-etching technique [64].

Funding. National Research Council Canada (NRC); Natural Sciences and Engineering Research Council of Canada (NSERC); National Institute for Nanotechnology (NINT); Canada Foundation for Innovation (CFI); Alberta Innovates – Technology Futures (AITF).

Acknowledgment. The authors would like to thank A. C. Hryciw for his assistance with this project.

See Supplement 1 for supporting content.

REFERENCES

1. P. Treutlein, C. Genes, K. Hammerer, M. Poggio, and P. Rabl, "Hybrid mechanical systems," in *Cavity Optomechanics* (Springer, 2014), pp. 327–351.
2. I. Aharonovich, A. D. Greentree, and S. Prawer, "Diamond photonics," Nat. Photonics **5**, 397–405 (2011).
3. E. R. MacQuarrie, T. A. Gosavi, N. R. Jungwirth, S. A. Bhave, and G. D. Fuchs, "Mechanical spin control of nitrogen-vacancy centers in diamond," Phys. Rev. Lett. **111**, 227602 (2013).
4. J. Teissier, A. Barfuss, P. Appel, E. Neu, and P. Maletinsky, "Strain coupling of a nitrogen-vacancy center spin to a diamond mechanical oscillator," Phys. Rev. Lett. **113**, 020503 (2014).
5. P. Ovartchaiyapong, K. W. Lee, B. A. Myers, and A. C. B. Jayich, "Dynamic strain-mediated coupling of a single diamond spin to a mechanical resonator," Nat. Commun. **5**, 4429 (2014).
6. A. Barfuss, J. Teissier, E. Neu, A. Nunnenkamp, and P. Maletinsky, "Strong mechanical driving of a single electron spin," Nat. Phys. **11**, 820–824 (2015).
7. S. Meesala, Y.-I. Sohn, H. A. Atikian, S. Kim, M. J. Burek, J. T. Choy, and M. Lončar, "Enhanced strain coupling of nitrogen-vacancy spins to nanoscale diamond cantilevers," Phys. Rev. Appl. **5**, 034010 (2016).
8. E. R. MacQuarrie, T. A. Gosavi, A. M. Moehle, N. R. Jungwirth, S. A. Bhave, and G. D. Fuchs, "Coherent control of a nitrogen-vacancy center spin ensemble with a diamond mechanical resonator," Optica **2**, 233–238 (2015).
9. O. Arcizet, V. Jacques, A. Siria, P. Poncharal, P. Vincent, and S. Seidelin, "A single nitrogen-vacancy defect coupled to a nanomechanical oscillator," Nat. Phys. **7**, 879–883 (2011).
10. D. A. Golter, T. Oo, M. Amezcua, K. A. Stewart, and H. Wang, "Optomechanical quantum control of a nitrogen-vacancy center in diamond," Phys. Rev. Lett. **116**, 143602 (2016).
11. K. W. Lee, D. Lee, P. Ovartchaiyapong, J. Minguzzi, J. R. Maze, and A. C. B. Jayich, "Strain coupling of a mechanical resonator to a single quantum emitter in diamond," arXiv:13603.07680 (2016).
12. M. Aspelmeyer, T. J. Kippenberg, and F. Marquardt, "Cavity optomechanics," Rev. Mod. Phys. **86**, 1391–1452 (2014).

13. S. Weis, R. Rivière, S. Deléglise, E. Gavartin, O. Arcizet, A. Schliesser, and T. J. Kippenberg, "Optomechanically induced transparency," Science **330**, 1520–1523 (2010).
14. A. H. Safavi-Naeini, T. M. Alegre, J. Chan, M. Eichenfield, M. Winger, Q. Lin, J. T. Hill, D. Chang, and O. Painter, "Electromagnetically induced transparency and slow light with optomechanics," Nature **472**, 69–73 (2011).
15. Y. Liu, M. Davanço, V. Aksyuk, and K. Srinivasan, "Electromagnetically induced transparency and wideband wavelength conversion in silicon nitride microdisk optomechanical resonators," Phys. Rev. Lett. **110**, 223603 (2013).
16. J. Chan, T. P. M. Alegre, A. H. Safavi-Naeini, J. T. Hill, A. Krause, S. Groblacher, M. Aspelmeyer, and O. Painter, "Laser cooling of a nanomechanical oscillator into its quantum ground state," Nature **478**, 89–92 (2011).
17. K. V. Kepesidis, S. D. Bennett, S. Portolan, M. D. Lukin, and P. Rabl, "Phonon cooling and lasing with nitrogen-vacancy centers in diamond," Physical Rev. B **88**, 064105 (2013).
18. P. Rabl, S. Kolkowitz, F. Koppens, J. Harris, P. Zoller, and M. Lukin, "A quantum spin transducer based on nanoelectromechanical resonator arrays," Nat. Phys. **6**, 602–608 (2010).
19. K. Stannigel, P. Rabl, A. S. Sørensen, P. Zoller, and M. D. Lukin, "Optomechanical transducers for long-distance quantum communication," Phys. Rev. Lett. **105**, 220501 (2010).
20. M. J. A. Schuetz, E. M. Kessler, G. Giedke, L. M. K. Vandersypen, M. D. Lukin, and J. I. Cirac, "Universal quantum transducers based on surface acoustic waves," Phys. Rev. X **5**, 031031 (2015).
21. I. Wilson-Rae, P. Zoller, and A. Imamoğlu, "Laser cooling of a nanomechanical resonator mode to its quantum ground state," Phys. Rev. Lett. **92**, 075507 (2004).
22. E. MacQuarrie, M. Otten, S. Gray, and G. Fuchs, "Cooling a mechanical resonator with a nitrogen-vacancy center ensemble using a room temperature excited state spin-strain interaction," arXiv:1605.07131 (2016).
23. T. Ramos, V. Sudhir, K. Stannigel, P. Zoller, and T. J. Kippenberg, "Nonlinear quantum optomechanics via individual intrinsic two-level defects," Phys. Rev. Lett. **110**, 193602 (2013).
24. P. Rath, S. Khasminskaya, C. Nebel, C. Wild, and W. H. Pernice, "Diamond-integrated optomechanical circuits," Nat. Commun. **4**, 1690 (2013).
25. Y. Tao, J. M. Boss, B. A. Moores, and C. L. Degen, "Single-crystal diamond nanomechanical resonators with quality factors exceeding one million," Nat. Commun. **5**, 3638 (2013).
26. G. Balasubramanian, P. Neumann, D. Twitchen, M. Markham, R. Kolesov, N. Mizuochi, J. Isoya, J. Achard, J. Beck, J. Tissler, V. Jacques, P. Hemmer, F. Jelezko, and F. Wrachtrup, "Ultralong spin coherence time in isotopically engineered diamond," Nat. Mater. **8**, 383–387 (2009).
27. E. Gil-Santos, C. Baker, D. Nguyen, W. Hease, A. Lematre, S. Ducci, G. Leo, and I. Favero, "High frequency nano-optomechanical disk resonators in liquids," Nat. Nanotechnol. **10**, 810–816 (2015).
28. X. Lu, J. Y. Lee, and Q. Lin, "High-frequency and high-quality silicon carbide optomechanical microresonators," Sci. Rep. **5**, 17005 (2015).
29. A. Faraon, P. E. Barclay, C. Santori, K.-M. C. Fu, and R. G. Beausoleil, "Resonant enhancement of the zero-phonon emission from a color center in a diamond cavity," Nat. Photonics **5**, 301–305 (2011).
30. P. Ovartchaiyapong, L. M. A. Pascal, B. A. Myers, P. Lauria, and A. C. B. Jayich, "High quality factor single-crystal diamond mechanical resonators," Appl. Phys. Lett. **101**, 163505 (2012).
31. M. J. Burek, N. P. de Leon, B. J. Shields, B. J. Hausmann, Y. Chu, Q. Quan, A. S. Zibrov, H. Park, M. D. Lukin, and M. Lončar, "Free-standing mechanical and photonic nanostructures in single-crystal diamond," Nano Lett. **12**, 6084–6089 (2012).
32. B. Khanaliloo, H. Jayakumar, A. C. Hryciw, D. P. Lake, H. Kaviani, and P. E. Barclay, "Single-crystal diamond nanobeam waveguide optomechanics," Physical Rev. X **5**, 041051 (2015).
33. M. J. Burek, Y. Chu, M. S. Z. Liddy, P. Patel, J. Rochman, S. Meesala, W. Hong, Q. Quan, M. D. Lukin, and M. Lončar, "High quality-factor optical nanocavities in bulk single-crystal diamond," Nat. Commun. **5**, 5718 (2014).
34. B. Khanaliloo, M. Mitchell, A. C. Hryciw, and P. E. Barclay, "High-Q/V monolithic diamond microdisks fabricated with quasi-isotropic etching," Nano Lett. **15**, 5131–5136 (2015).
35. P. Maletinsky, S. Hong, M. S. Grinolds, B. Hausmann, M. D. Lukin, R. L. Walsworth, M. Lončar, and A. Yacoby, "A robust scanning diamond sensor for nanoscale imaging with single nitrogen-vacancy centres," Nat. Nanotechnol. **7**, 320–324 (2012).
36. C. P. Michael, M. Borselli, T. J. Johnson, C. Chrystala, and O. Painter, "An optical fiber-taper probe for wafer-scale microphotonic device characterization," Opt. Express **15**, 4745–4752 (2007).
37. M. Mitchell, A. C. Hryciw, and P. E. Barclay, "Cavity optomechanics in gallium phosphide microdisks," Appl. Phys. Lett. **104**, 141104 (2014).
38. M. Borselli, K. Srinivasan, P. E. Barclay, and O. Painter, "Rayleigh scattering, mode coupling, and optical loss in silicon microdisks," Appl. Phys. Lett. **85**, 3693–3695 (2004).
39. D. T. Nguyen, C. Baker, W. Hease, S. Sejil, P. Senellart, A. Lemaître, S. Ducci, G. Leo, and I. Favero, "Ultrahigh Q-frequency product for optomechanical disk resonators with a mechanical shield," Appl. Phys. Lett. **103**, 241112 (2013).
40. R. Rivière, "Cavity optomechanics with silica toroidal microresonators down to low phonon occupancy," Ph.D. thesis (Ludwig-Maximilians-Universität München, 2011).
41. X. Sun, X. Zhang, and H. X. Tang, "High-q silicon optomechanical microdisk resonators at gigahertz frequencies," Appl. Phys. Lett. **100**, 173116 (2012).
42. M. Eichenfield, J. Chan, R. Camacho, K. Vahala, and O. Painter, "Optomechanical crystals," Nature **462**, 78–82 (2009).
43. K. Ekinci, Y. Yang, and M. Roukes, "Ultimate limits to inertial mass sensing based upon nanoelectromechanical systems," J. Appl. Phys. **95**, 2682–2689 (2004).
44. W. Yu, W. C. Jiang, Q. Lin, and T. Lu, "Cavity optomechanical transduction sensing of single molecules," arXiv:1504.03727 (2015).
45. C. T.-C. Nguyen, "Mems technology for timing and frequency control," IEEE Trans. Ultrason. Ferroelectr. Freq. Control **54**, 251–270 (2007).
46. R. A. Norte, J. P. Moura, and S. Gröblacher, "Mechanical resonators for quantum optomechanics experiments at room temperature," Phys. Rev. Lett. **116**, 147202 (2016).
47. W. Li, N. Mingo, L. Lindsay, D. A. Broido, D. A. Stewart, and N. A. Katcho, "Thermal conductivity of diamond nanowires from first principles," Physical Rev. B **85**, 195436 (2012).
48. D. Li, Y. Wu, P. Kim, L. Shi, P. Yang, and A. Majumdar, "Thermal conductivity of individual silicon nanowires," Appl. Phys. Lett. **83**, 2934–2936 (2003).
49. B. J. Hausmann, I. Bulu, V. Venkataraman, P. Deotare, and M. Lončar, "Diamond nonlinear photonics," Nat. Photonics **8**, 369–374 (2014).
50. J. Chan, A. Safavi-Naeini, J. Hill, S. Meenehan, and O. Painter, "Optimized optomechanical crystal cavity with acoustic radiation shield," Appl. Phys. Lett. **101**, 081115 (2012).
51. L. S. Hounsome, R. Jones, M. J. Shaw, and P. R. Briddon, "Photoelastic constants in diamond and silicon," Phys. Status Solidi A **203**, 3088–3093 (2006).
52. D. T. Nguyen, W. Hease, C. Baker, E. Gil-Santos, P. Senellart, A. Lemaître, S. Ducci, G. Leo, and I. Favero, "Improved optomechanical disk resonator sitting on a pedestal mechanical shield," New J. Phys. **17**, 023016 (2015).
53. J. R. Clark, W.-T. Hsu, M. A. Abdelmoneum, and C. T.-C. Nguyen, "High-Q UHF micromechanical radial-contour mode disk resonators," J. Microelectromech. Syst. **14**, 1298–1310 (2005).
54. R. Yang, Z. Wang, J. Lee, K. Ladhane, D. J. Young, and P. X. L. Feng, "Temperature dependence of torsional and flexural modes in 6H-SiC microdisk resonators," in *IEEE International Frequency Control Symposium (FCS)* (2014), pp. 1–3.
55. W. C. Jiang, X. Lu, J. Zhang, and Q. Lin, "High-frequency silicon optomechanical oscillator with an ultralow threshold," Opt. Express **20**, 15991–15996 (2012).
56. J. Hodges, L. Li, M. Lu, E. H. Chen, M. Trusheim, S. Allegri, X. Yao, O. Gaathon, H. Bakhru, and D. Englund, "Long-lived NV- spin coherence in high-purity diamond membranes," New J. Phys. **14**, 093004 (2012).
57. N. Bar-Gill, L. Pham, A. Jarmola, D. Budker, and R. Walsworth, "Solid-state electronic spin coherence time approaching one second," Nat. Commun. **4**, 1743 (2013).
58. G. Davies and M. F. Hamer, "Optical studies of the 1.945 eV vibronic band in diamond," Proc. R. Soc. London A **348**, 285–298 (1976).

59. A. Batalov, V. Jacques, F. Kaiser, P. Siyushev, P. Neumann, L. J. Rogers, R. L. McMurtrie, N. B. Manson, F. Jelezko, and J. Wrachtrup, "Low temperature studies of the excited-state structure of negatively charged nitrogen-vacancy color centers in diamond," Phys. Rev. Lett. **102**, 195506 (2009).
60. C. Baker, W. Hease, D.-T. Nguyen, A. Andronico, S. Ducci, G. Leo, and I. Favero, "Photoelastic coupling in gallium arsenide optomechanical disk resonators," Opt. Express **22**, 14072–14086 (2014).
61. C. Dong, V. Fiore, M. C. Kuzyk, and H. Wang, "Optomechanical dark mode," Science **338**, 1609–1613 (2012).
62. J. T. Hill, A. H. Safavi-Naeini, J. Chan, and O. Painter, "Coherent optical wavelength conversion via cavity optomechanics," Nat. Commun. **3**, 1196 (2012).
63. K. Stannigel, P. Komar, S. J. M. Habraken, S. D. Bennett, M. D. Lukin, P. Zoller, and P. Rabl, "Optomechanical quantum information processing with photons and phonons," Phys. Rev. Lett. **109**, 013603 (2012).
64. M. J. Burek, J. D. Cohen, S. M. Meenehan, T. Ruelle, S. Meesala, J. Rochman, H. A. Atikian, M. Markham, D. J. Twitchen, M. D. Lukin, O. Painter, and M. Lončar, "Diamond optomechanical crystals," arXiv:1512.04166 (2015).